UNIVERSITY
OF TRENTO - Italy
Department of Physics

NANOSCIENCE LABORATORY

HIGHLIGHTS 2016

Image on the front cover:
The photonic quantum chip: design by NL and fabrication by FBK-CMM. Photo by S. Signorini e C. Castellan.

NANOSCIENCE LABORATORY

MEMBERS (2016)

Faculty staff

Lorenzo Pavesi (full professor, head)
Marina Scarpa (full professor)
Zeno Gaburro (associate professor)
Paolo Bettotti (assistant professor)
Fernando Ramiro Manzano (researcher)

Technical staff

Enrico Moser
Giorgio Fontana (EP7 level)

Administrative staff

Tatsiana Yatskevich

Post-doctoral fellows

Mattia Mancinelli
Massimo Borghi

Doctoral students

Fabio Turri
Zahra Bisadi
Stefano Tondini
Tatevik Chalyan
Alessandro Trenti
Claudio Castellan
Cecilia Ada Maestri
Chiara Piotto
Stefano Signorini
Sara Piccione
Stefano Biasi
Astghik Chalyan (Guest PhD student)
Foroogh Sarbishe Khozeymeh (Guest PhD student)

Master students

Alessandro Marchesini
Niccolò Carlino
Alessio Lugnan
Mattia Cominelli
Giovanni Visonà
Alessandra Vendrame
Francesca Marchetti

SCIENTIFIC MISSION

Introduction to the Nanoscience Laboratory

The Nanoscience Laboratory (NL) is one of the scientific groups of the Department of Physics, University of Trento. Its main areas of research are integrated quantum photonics, linear and nonlinear silicon photonics and nanobiotechnologies. The mission of NL is to generate new knowledge, to develop understanding and to spin-off applications from physical phenomena associated with photons and nanostructures. In particular, NL works on applying the nanoscience paradigm to silicon or silicon compatible materials to develop micro and nanosystems compatible with the main driving silicon microelectronics technologies. However, silicon is not the only material studied. Other fields of interest concern the use of cellulose to tailor the properties of nanostructure atom-by-atom or the use of perovskites to investigate their new properties. In addition, a particular emphasis is placed on quantum photonics and its applications.
NL research group consists of more than 20 people with different scientific backgrounds. Researchers from physics, bio-chemistry, materials science and electrical engineering are gathered to form a group of interdisciplinary nature. It is worth mentioning that NL collaborates closely with the Center of Materials and Microsystems, Fondazione Bruno Kessler (FBK). This collaboration spans over the last twenty years and covers such topics as fabrication, testing and application of biomaterials and silicon based devices. Both participate in many common projects. The current ones are: project "On silicon chip quantum optics for quantum computing and secure communications – SiQuro" (financed by the Province of Trento (PAT)) and the project "Integrated SYsteM based on PHOtonic Microresonators and Microfluidic Components for rapid detectioN of toxins in milk and diarY products – SYMPHONY" (financed by the European Commission within the 7th framework). A new tight collaboration is ongoing with the Trento units of CNR-INO, specifically dedicated to implement quantum optics in integrated chip.
Moreover, with the support of FBK and CNR, every two years NL organizes a winter school on optoelectronics and photonics. The next edition will be the "9th Optoelectronics and Photonics Winter School: Integrated Quantum Photonics" (March 2017). Furthermore, the members of NL are often invited to participate in the organizing committees of

international conferences or workshops.
The research activities of NL are mainly supported by the local government (PAT), by the European Commission within the research frameworks, by the Italian Ministry of Education, University and Research (MIUR) and by companies. During the period covered by these Highlights, NL has been and is involved in the following projects: Project FIRB NEMATIC "Nanoporous matErials: self asseMbled blAckboard to study sTructure and InteraCtions of DNA, project SiQuro (supported by PAT within the call Grandi Progetti 2012), project PRIN-MIUR NEMO "Nonlinear dynamics of optical frequency combs", some European projects within the 7th Framework: SYMPHONY (FP7-ICT-2013-10) and "Integrated Reconfigurable sIlicon phonic Switch – IRIS" (FP7-ICT-2013-11).

Silicon Nanophotonics

Silicon photonics is the technology where photonic devices are produced by standard microelectronic processes using the same paradigm of electronics: integration of a large number of devices to yield a high circuit complexity, which allows for high performances and low costs. Here, the truth is to develop photonic devices that can be easily integrated to improve the single device performance and to allow high volume production.
We are involved in researching new optical scheme for implementing optical network on a chip by using integrated silicon photonics. Thousands of electrical and optical devices are integrated in a single chip to make reconfigurable optical network. We use the concept of whispering gallery modes, which develop in micro-disks or micro-rings, to study new physics (chirality, frequency comb generation, entangled photon generation) or to develop biosensors for toxin detections. The microresonators are coupled directly with narrow mode SOI (Silicon-on-Insulator) waveguides. High quality factor cavities allow studying fundamental quantum optics concept such Bogoliubov excitation in quantum fluid of light. Series of coupled micro-rings are studied to implement novel scheme of neuromorphic computers where the complex dynamic of the nonlinear resonators allows fast and efficient pattern recognition.
To develop silicon photonics, one further add-on is making silicon to do something that it is not able to do in its standard (bulk) form. Low dimensional silicon, where small silicon nanocrystals or nanoclusters (Si-nc) are developed, is one way to compel silicon to act as an active optical material. Alternatively, we use the strain to tune the non-linear optical properties of silicon waveguides for the development of new MIR sources (parametric generation via second order effects or frequency comb generation). Nonlinear optics is used to generate pairs of entangled photons, which in turn feed quantum interferometers or integrated quantum photonic circuits. Here, a large effort is spent in order to demonstrate in integrated devices the new properties of quantum fluid of light where the nonlinear photon-photon interaction modify the classical properties of light.

Nanobiotechnologies, antioxidants and human health

All the aspects related to the nano-bio interfaces (which are the structures where the co-existence of physical principles and biological molecules is clearly evident) are a challenging field of research. Though the leading research concerns the design, synthesis and dynamic behavior of nano-structured bio-interfaces, more specifically we are working on three research topics: silicon- and titanium based nanosystems, single molecule detection, and antioxidant behavior in micelle systems, polymers and nanoporousporous structures. .
To develop silicon based bio-sensors, we are currently focused on silicon based hybrid nanostructures. In particular silicon or silicon nitride flat or porous films are the starting inorganic support into which bio active layers are designed. Biological recognition elements are introduced on this hybrid layer. Molecular surface density, active layer thickness and integration of the bio-active interface with photonic devices will be the future challenges to develop the sensor system. In addition, we are developing nanostructured hybrid interfaces to capture bio-analytes and enhance their Raman signals. Gold and silver nanoparticles are used as enhancers. Beyond traditional sensor applications, silicon nanostructures can be used as "nanosensors", which monitor the intracellular events without introducing irreversible perturbations. To this regard light emitting silicon quantum dots appear very promising. We are studying the nanoparticle coating to increase optical stability and decrease toxicity, moreover conjugation to biological molecules and strategies to increase cell uptake and control intracellular localization are future steps of this research. Titanium nanotubes showing hydroxyl-rich interfaces have been synthesized. These nanosystems are easily dispersed and stable in aqueous solutions and show a high photocatalytic activity.

Experimental facilities

The NL facilities allow for detailed experimental studies in nanoscience, photonics and biotechnologies. Since the effective collaboration with FBK most material processing and device productions are performed within their premises. For photonics, we have facilities to cover the light spectrum from the THz to UV ranges with whatever time resolution is needed. Laser sources comprehends: Ti-sapphire fs-ps laser (1 W average over 1000-700 nm, 2 ps or 70 fs pulses, 82 MHz repetition rate) interfaced with a second harmonic generator and pulse picker; Nd-Yag laser interfaced with an optical parametric oscillator which allows scanning the 400-3000 nm wavelength region (pulse 50 mJ, 10 ns, 10 Hz); TOPAS pumped with an amplified Ti:Sa laser which covers the 1-2.6 μm range with 35 fs, 10 kHz, 3 mJ; three tunable CW lasers (850-870 nm, 1200 - 1700 nm and 1500 - 1600nm) fiber pig-tailed; high power fiber-laser at 1550 nm (1-100 MHz, 50 ps); 4W EDFA and 2W semiconductors amplifiers, several pig-tailed diode lasers, ASE source at 1550 nm and a broad band SLD at 800 nm; three high-power true-CW DPSS single-line laser operating at 532, 473 and 355 nm. Detectors comprehend: visible and infrared photomultipliers and CCDs, a streak camera with ps resolution, 4K cooled bolometers which cover THz region, avalanche photodiodes for vis and IR ranges plus single photon detectors in the visible and IR. Two home-made MIR single photo counters. To perform spectral analysis several set-ups are available: FTIR and dispersive spectrophotometers, a micro-Raman setup, a micro-FTIR and a UV-vis-IR spectrophotometer (shared with other laboratories), UV-Vis and fluorescence spectrophotometer dedicated to biochemical experiments. Seven dedicated apparata for WG characterization equipped with nanopositioning systems and polarization controllers are available, each one specified on a given functions: visible, quantum, passive infrared, nonlinear infrared, nonlinear MIR, and on-wafer grating. Other apparata are: - visible and infrared photoconductivity set-up; - a solar simulator for cell sizes up to 5 inches; - two nanoprobe stations (AFM and SNOM) - two semiconductor probe stations (4 and 8 inches) and many different electrical characterization set-ups (I-V, Z-Ω, EL-I, etc.). Two VIS to NIR optical spectrum analyzers are available to NL-Lab. A probe station is fiber-bunch interfaced with a spectrometer interfaced with IR and visible liquid nitrogen cooled CCDs. For sample treatment and high sensitivity analytical detection, an electrochemical laboratory equipped with several chemical hots, spinners, galvanostates and voltammeters is available. For optical, electrical and molecular dynamic simulations, the laboratory uses free and commercial software, a dedicated cluster with 16 nodes and work-stations. Two laboratories, one dedicated to chemical synthesis and the second to biological sample preparation, are also available.

2016 publications

- P. Bettotti, C.A. Maestri, R. Guider, I. Mancini, E. Nativ-Roth, Y. Golan, M. Scarpa, M., "Dynamics of Hydration of Nanocellulose Films", Advanced Materials Interfaces 3(5), 1500415 (2016).
- R. Guider, C. Traversa, P. Bettotti "Mechanical stress relief in porous silicon free standing membranes", Opt. Mater. Express, 5(10), 2128-2135(2015).
- P. Bettotti, N. Kumar, R. Guider, M. Scarpa, M., "Optical sensors based on nanoporous materials", Lecture Notes in Electrical Engineering, 319, 103-107(2015).
- G. G. Daaboul, P. Gagni, L. Benussi, P. Bettotti, M. Ciani, M. Cretich, D. S. Freedman, R. Ghidoni, A. Yalcin Ozkumur, C. Piotto, D. Prosperi, B. Santini, M. Selim Ünlü & M. Chiari "Digital Detection of Exosomes by Interferometric Imaging" Scientific Reports, 6, 37246 (2016)
- F. Sgrignuoli and P. Bettotti "Roughness-induced enhancement of optical absorption in random media" J. Optical Society of America B 33 (5), 915-921 (2016).
- Z. Bisadi, A. Meneghetti, A. Tomasi, G. Fontana, A. Tengattini, G. Pucker, P. Bettotti, M. Sala, L. Pavesi "Generation of high quality random numbers via an all-silicon-based approach" physica status solidi (a) 213, 3186–3193 (2016).
- A. Trenti, M. Borghi, M. Mancinelli, G. Fontana, and L. Pavesi "Quantum interference in an asymmetric Mach-Zehnder Interferometer" Journal of Optics 18, 085201 (2016).
- T. Chalyan, R. Guider, L. Pasquardini, M. Zanetti, F. Falke, E. Schreuder, R. G. Heideman, C. Pederzolli and L. Pavesi "Asymmetric Mach-Zehnder Interferometer based biosensors for Aflatoxin M1 detection", Biosensors 6(1), 1 (2016).
- A. Samusenko, D. Gandolfi, G. Pucker, T. Chalyan, R. Guider, M. Ghulinyan, and L. Pavesi "A SiON microring resonator-based platform for biosensing at 850 nm", IEEE Journal of Lightwave Technology 34, 969-977 (2016)
- C. Castellan, S. Tondini, M. Mancinelli, C. Kopp, and L. Pavesi "Reflectance reduction in a whiskered SOI star coupler", IEEE Photonics Technology Letters 28, 1041-1135 (2016).
- F. Testa, C. J. Oton, C. Kopp, J-M. Lee, R. Ortuño, R. Enne, S. Tondini, G. Chiaretti, A. Bianchi, P. Pintus, M. Kim, D. Fowler, J. Ayucar, M. Hofbauer, M. Mancinelli, M. Fournier, G. B. Preve, N. Zecevic, C. Manganelli, C. Castellan, G. Pares, O. Lemonnier, F. Gambini, P. Labeye, M. Romagnoli, L. Pavesi, H. Zimmerman, F. Di Pasquale, S. Stracca, "Design and Implementation of an Integrated Reconfigurable Silicon Photonics Switch Matrix in IRIS Project", Journal of Selected Topics in Quantum Electronics 22, 3600314 (2016).
- S. Manna, M. Bernard, S. Biasi, F. Ramiro Manzano, M. Mancinelli, M. Ghulinyan, G. Pucker, L. Pavesi, "Stimulated degenerate Four-Wave Mixing in Si nanocrystals waveguides", Journal of Optics 18, 075801(2016)
- S. Tondini, G. Pucker, and L. Pavesi "Role of the inversion layer on the charge injection in silicon nanocrystal multilayered light emitting devices", Journal of Applied Physics 120, 093108 (2016).
- Tatevik Chalyan, Laura Pasquardini, Davide Gandolfi,

Romain Guider, Alina Samusenko, Manuela Zanetti, Georg Pucker, Cecilia Pederzolli, and Lorenzo Pavesi "Aptamer- and Fab'- functionalized microring resonators for Aflatoxin M1 detection", IEEE Selected Topics in Quantum Electronics 23, 5900208 (2016).
- Massimo Borghi, Mattia Mancinelli, Martino Bernard, Mher Ghulinyan, Georg Pucker and Lorenzo Pavesi, "Homo-dyne detection of free carrier induced electro-optic modulation in strained silicon resonators", IEEE Journal of Lightwave technology 34, 5657-5668 (2016)
- Fabio Turri, Fernando Ramiro-Manzano, Iacopo Carusotto, Mher Ghulinyan, Georg Pucker, and Lorenzo Pavesi, "Wavelength dependence of a vertically coupled resonator-waveguide system" Journal of Lightwave Technology 34, 5385 (2016).
- Tatevik Chalyan, Laura Pasquardini, Floris H. Falk, Manuela Zanet, Romain Guider, Davide Gandolfi, Erik Schreuder, Cecilia Pederzolli, Rene G. Heideman, and Lorenzo Pavesi "Biosensors based on Si3N4 Asymmetric Mach-Zehnder Interferometers" Proc. SPIE 9899, Optical Sensing and Detection IV, 98991S (2016).
- A. Trenti, M. Borghi, M. Mancinelli, H. M. Price, G. Fontana, and L. Pavesi "One and two photon quantum interference in a Mach-Zehnder interferometer" Proc. SPIE 9894, Nonlinear Optics and its Applications IV, 98940W (2016).
- Massimo Borghi, Mattia Mancinelli, Florian Merget, Jeremy Witzens, Martino Bernard, Mher Ghulinyan, Georg Pucker and Lorenzo Pavesi "High frequency electro optic measurement of strained silicon racetrack resonators" Proc. SPIE 9891, Silicon Photonics and Photonic Integrated Circuits V, 98910D (2016).
- Stefano Tondini, Claudio Castellan, Mattia Mancinelli, and Lorenzo Pavesi "Modelling and validation of high-performance and athermal AWGs for the silicon photonics platform" Proc. SPIE 9891, Silicon Photonics and Photonic Integrated Circuits V, 98910C (2016).
- F. Ramiro-Manzano, S. Biasi, M. Bernard, M. Mancinelli, T. Chalyan, F. Turri, M. Ghulinyan, M. Borghi, A. Samusenko, D. Gandolfi, R. Guider, A. Trenti, P.-É. Larré, L. Pasquardini, I. Carusotto, G. Pucker, and L. Pavesi "Resonators and Silicon Photonics", MRS Advances, 1(48) 3281-3293 (2016).
- Z. Bisadi, P. Cortelletti, A. Zanzi, C. Piotto, G. Fontana, P. Bettotti, M. Scarpa, L. Pavesi "Silicon Nanostructures: a versatile material for photonics" (invited) ECS Transactions, 72(34), 1-6 (2016)
- Z. Bisadi, G. Fontana, E. Moser, G. Pucker, L. Pavesi "A robust approach to the generation of high quality Random Numbers" Proc. SPIE 9996, Quantum Information Science and Technology II, 99960P (2016).
- Gaburro Z., Daldosso N., and Pavesi L., Porous Silicon. In: Saleem Hashmi (editor-in-chief), Reference Module in Materials Science and Materials Engineering. Oxford: Elsevier; 2016. pp. 1-11 (doi:10.1016/B978-0-12-803581-8.01134-6)

2016 PhD Thesis:

Massimo Borghi "*Linear, nonlinear and quantum optics in Silicon Photonics*" (21st of March, 2016)

2016 books:

Silicon Photonics III: Systems and Applications, Lorenzo Pavesi and David J. Lockwood editors, Topics in Applied Physics vol 122 (2016)

Silicon Photonics and Photonic Integrated Circuits V, editors Laurent Vivien, Lorenzo Pavesi, Stefano Pelli, Proc. SPIE 9891 (April 3, 2016).

1. Robust Quantum Random Number Generation with Si-NCs LLED and SiPM Compact Configuration (Zahra Bisadi, Giorgio Fontana)

In order to develop an integrated Quantum Random Number Generator within the SIQURO project, we made up a setup comprising a Si-NCs large area LED (LLED) and a Si photomultiplier (SiPM) (Fig. 1). Si-NCs LLEDs were fabricated in FBK to illuminate completely the large area SiPM detectors. The Si-NCs LLED has a multilayer structure with 5 periods of 3.5-4 nm silicon rich oxide (SRO) sandwiched between SiO_2 layers of 2 nm thickness.

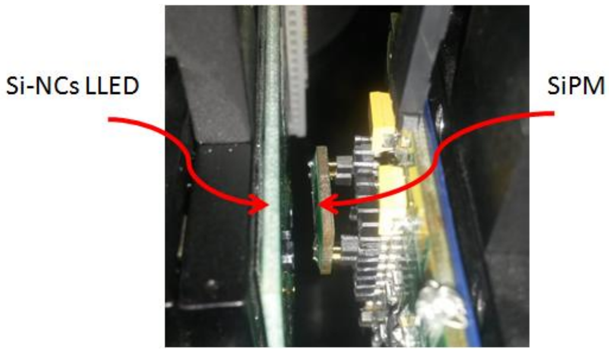

Figure 1. *The compact configuration comprising Si-NCs LLED (on the left) and SiPM (on the right)*

The EL spectra of these LLEDs had a peak at ~850 nm due to the emission from Si-NCs. The measurements for random number generation were performed on a Si-NCs LLED with an active area of 0.99 x 0.82 mm^2 suitable to be coupled with the large area SiPM with the dimension of 1 x $1mm^2$.

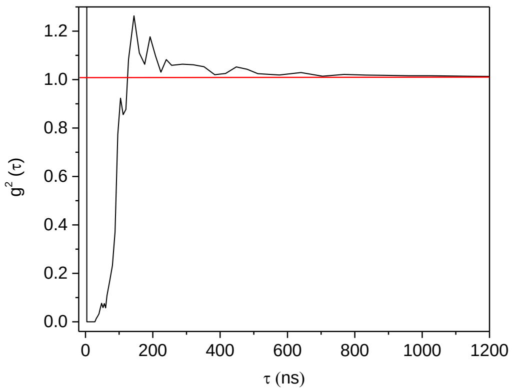

Figure 2. *Autocorrelation function ($g^2(\tau)$) of the SiPM signal (peak at zero is out of scale). Dead time and afterpulsing distribution of the detector can be seen here*

The experimental setup consists of Si-NCs LLED as the quantum source of entropy, SiPM as the detector and field-programmable gate array (FPGA) for random number extraction. The photons emitted from the Si-NCs LLED are detected by SiPM and then the electrical signal is transmitted to the FPGA where random hexadecimal symbols are generated. The autocorrelation, $g^2(\tau)$, measurement of the SiPM signal was performed via a multitau digital correlator with 4 ns resolution. The afterpulsing distribution exhibits a main peak within 140 ns from the main autocorrelation peak at τ=0. The plateau in $g^2(\tau)$ approaches the normalization value of 1 at about 950 ns.

Considering the $g^2(\tau)$, we set the length of the "double length interval" (see Fig. 3) to 1920 ns—with the first half of Ns to be 960 ns that is long enough to mask the afterpulsing and crosstalk distribution of SiPM (see Fig. 2).

Setting the "double length interval" to 1920 ns, we acquired long sequences of datasets. The generated raw data show high quality of randomness. The analysis of joint probability mass function (JPMF), shows a very low deviation in the order of 10^{-6} from the expected theoretical value of (1/16)x(1/16)=0.00390625. The mutual information (MI) of the generated random symbols is calculated to be ~10^{-7} bits considering 1G random symbols.

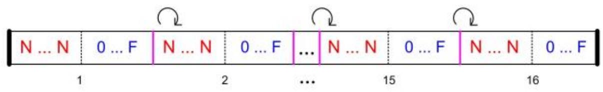

Figure 3. *Target function for random hexadecimal symbols extraction. The "super interval" is composed of 16 "double length interval" with the first half of Ns (no number) and the second half of alternate Ns and hexadecimal symbols. There is a consecutive one-rotation in hexadecimal symbols in each "double length interval" shown by circular arrows in the figure*

The maximum bias is calculated to be in the order of 10^{-5} and the mean entropy is ~ 3.9997 bits per nibble or 4-bits. The highest bit-rate is calculated to be ~ 0.5 Mbps at the EL intensity of ~ 550 kHz. NIST tests for 2 Gbits of raw data show perfect randomness of the generate bit sequences. A comparison of the compact configuration with Si-NCs LLED and SiPM and the configuration with the Si-NCs LED and a commercial Perkin Elmer SPAD is presented in Table 1.

Property	*Si-NCs LED+SPAD*	*Si-NCs LLED+SiPM*
PDE*	45% @830 nm	20% @800 nm
Detection area	0.0254 mm^2	1 mm^2
DCR**	~ 300 Hz	~ 80 kHz
Current density	0.2-0.4 mA/cm^2	0.8-1.2 mA/cm^2
Robustness	Robust	Robust
Compactness	Bulky	Compact
Min-entropy	~3.999 bits per 4-bits	~ 3.999 bits per 4-bits
Bias	~ 10^{-5}	~ 10^{-5}
MI***	~ 10^{-7} bits	~ 10^{-7} bits
Bit-rate	~ 1.68 Mbps	~ 0.5 Mbps

*Photon Detection Efficiency, ** Dark Count Rate. ***Mutual Information

Table 1*. A comparison of the compact configuration with Si-NCs LLED and large area SiPM and the configuration with Si-NCs LED and the commercial Perkin Elmer SPAD (Z. Bisadi et al. IEEE J. Lightwave Technol. in press)*

2. Organic-inorganic hybrid halide perovskite deposited over flexible substrates for optoelectronic applications (Niccolò Carlino, Paolo Bettotti)

The project, realized in collaboration with the Institute of Advanced Materials of Universitat Jaume I (Spain), aims to develop a reliable procedure to deposit a perovskite layer onto flexible substrates and to study the optoelectronic properties of the structure. The fabrication of such hybrid device might be functional to the development of laser, led and photovoltaic cells and the use of flexible substrates can be a further degree of freedom to tune the properties of the active material, other than an important factor for expanding its applications.
The hybrid lead halide perovskite combines the advantage of organic materials, such as low costs, flexibility, simple and economic processing, tuning of optical and electrical properties, with that typical of inorganic materials (e.g. high charge-carrier mobility, high efficiency). Particularly, they have experienced an unprecedented breakthrough in the field of photovoltaics from 2012, reaching now the remarkable power conversion efficiency above 22%, comparable with commercial silicon-based devices. Moreover, the state of the art reports perovskite based multi-coloured light emitting diodes and optically pumped lasers, among its most important applications.

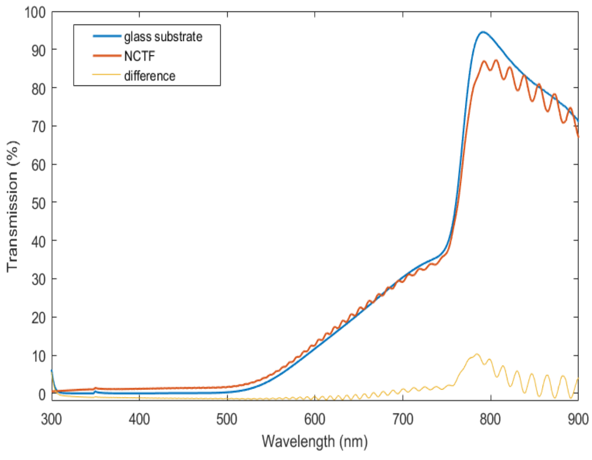

Figure 4. *Transmission spectrum of a MAPbI3 layer deposited on different substrates. The wave-like region is due to the interference generated by the thin NCTF.*

Organic-inorganic hybrid halide perovskites are crystals with the structure ABX3, where A is an organic cation, B is the metal cation and X is the halide anion. Among this vast class of materials, the most studied composition is the MAPbI3, where MA is methillamonium, a molecule with formula CH3NH3. Because of the choice of the single components, these materials offer a high tunability of both the bandgap and the crystal size. Justifying the unique development of this research field are the perovskites optoelectronic properties, such as long carrier diffusion length, high carrier mobility, and low trap density of states, which, in some cases, are already comparable with the longer-studied inorganic semiconductors. Moreover they show ambipolar conductivity and low exciton influence on absorption at photovoltaic carrier density regimes. Perovskites show a sharp optical absorption onset, described by a low Urbach energy, and symptom of a high crystalline purity. The absorption coefficient can reach values as high as 10^4 cm^{-1} near the band edge, usually positioned near 750-800 nm. This incredible value explain why perovskite-based solar cell have thicknesses in the order of hundreds of nanometers, whereas silicon solar cells need hundreds of microns and GaAs tenth of microns.
Most of our research is, hence, aimed to the understanding of perovskite characteristics and their origins, given that, despite the hype surrounding these materials, many of their properties are still unexplained. A further step is the search of a link between its performances and the different fabrication processes and methods.

3. Nanocellulose: structures and properties (Cecilia Ada Maestri, Marina Scarpa and Paolo Bettotti)

Cellulose is a structural polysaccharide representing the most abundant organic polymer on earth. Recently, there has been huge interest in the isolation of new forms of cellulose, with one dimension in the nanometer range. This new biomaterial is usually referred to as nanocellulose. The combination of mechanical strength, high degree of functionality and biocompatibility renders it a versatile platform as sustainable future material for applications in many different fields.
In our lab, we study this material in different forms and environments focusing on its dynamical properties and with particular attention on its structures and molecular organizations. Our aim is to understand the molecular structures and events at the basis of nanocellulose properties and in parallel exploit them for practical applications.
The first step is the physical-chemical preparation of cellulose nanofibers (Fig. 5) starting from cellulose soft pulp. Using aqueous suspensions of cellulose nanofibers, different nanocellulose-based materials can then be obtained.
We are, on one side, studying nanocellulose in the form of transparent films obtained by a casting procedure (fig. 5b). In particular, we are interested in investigating their structure and interaction with small molecules and to explain how these are related to some nanocellulose peculiar properties like actuation mechanisms and gas barrier properties.

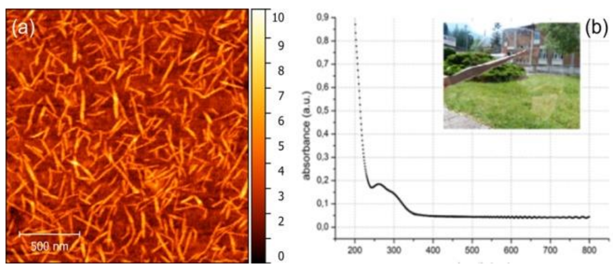

Figure 5. *(a) Atomic Force Microscopy image of cellulose nanofibers. (b) UV-VIS spectrum of a 20 μm thick transparent nanocellulose film (photograph in the inset).*

On the other side, we observed that cellulose nanofibers in aqueous solution containing small charged molecules tend to organize themselves forming stable gels with impressive mechanical properties (Fig. 6). We are now investigating this phase transition from liquid to gel with different experimental techniques (rheology, nuclear magnetic resonance, infrared spectroscopy and small angle X-ray scattering).

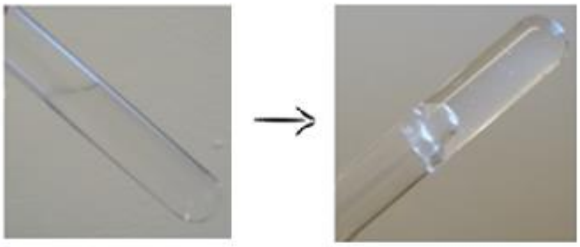

Figure 6. *Sol-gel transition from an aqueous nanocellulose solution to a transparent self-standing nanocellulose hydrogel.*

4. Porous Silicon for Drug Delivery (Chiara Piotto, Marina Scarpa and Paolo Bettotti)

Drug delivery (DD) refers to approaches and systems designed to transport and deliver the pharmaceutical compounds to the target organ in the body.
Drug carriers are useful because they protect the drugs from the degradation until the active ingredients reach the desired site, they reduce drug toxicity and give rise to a more efficient drug distribution; moreover they allow drugs to easily cross some barriers present in our body.
Among the various materials that are suitable for DD we use Porous silicon (Psi), a versatile material that, despite being known since several decades, is still matter of lively research and new technological applications are constantly demonstrated.

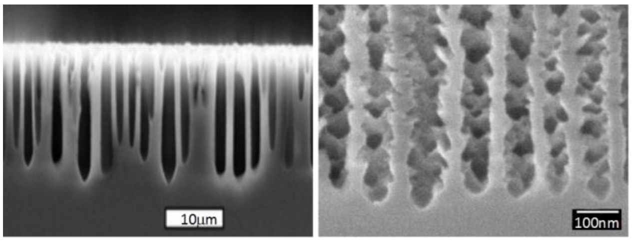

Figure 7. *SEM images that represent the Psi samples cross section: changing the etching parameters different morphologies can be obtained*

Exploiting an electrochemical corrosion process, it is possible to obtain various Psi nanostructures with different pore dimensions and shape (as reported in Fig. 7). Its porosity can reach 80% and its high surface to volume ratio allow high drug loading capacity. Its surface chemistry can be tune using simple functionalization reactions (in particular hydrosilylation and silanization), that render the surface hydrophilic or hydrophobic. Moreover, Psi can resist the heat and the harsh stomach conditions; another property is that once it is reduced down to nanosize, it becomes an efficient light emitting material.
All these characteristics and the fact that it is considered a biocompatible and biodegradable material have motivated its use for DD applications. As model drug, we use beta-carotene (BC), since it is small and hydrophobic as several drugs. We load the Psi chips depositing a known amount of a BC solution on the Psi surface: the capillary action draws the solution into the pores (impregnation method). Alternatively, we used cobinamide which is a vitamin B12 analogue and behaves as a probe of the red-ox activity of Psi. With both the model drugs, the drug stability, the loading amount and the release profile have been investigated. Analysing the BC release from various PSi substrates, we obtained different (fickian and NON-fickian) drug release kinetics depending on the PSi morphology, as reported in Fig. 8.

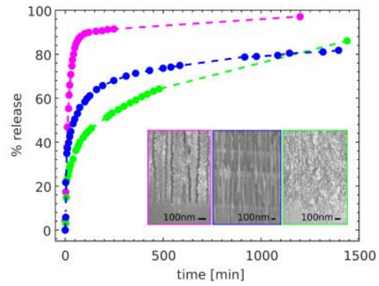

Figure 8. *BC release from Psi with different morphologies: if Psi with pores characterized by a diameter of 50nm are used the BC release is very fast and fickian diffusion is obtained; instead, if nano-sized pores are used, the release kinetics is slow down and cannot be fitted with a fickian law*

These are preliminary results obtained using Psi substrates, but the final goal is to use Psi particles, whose dimensions range from nano to micron size. With Psi particles one can obtain targeted DDS (if specific ligands, able to deliver the drugs at the desirable site, are attached on the Psi particles), controlled DDS (when a coverage on the Psi particles is created, so that the drugs are released at predetermined rate, in order to prolong the therapeutic effect) and smart DDS (if Psi particles are covered with materials that respond to chemical, physical or biological stimuli so that the active ingredients are released only after the carriers have received the proper stimulus).
By using cobinamide, which is a red-ox sensitive model drug, we noticed that naked PSi induces some drug degradation. Conversely, if PSi is opportunely functionalized, no drug deterioration is observed, the loading capacity is ameliorated and the optical stability is increased [1]. These results encourage us to try innovative functionalization procedures. In particular we are investigating space selective functionalization procedures of the pore surfaces [2]. Another interesting route to stabilize PSi surface is the thermal oxidation. In this regard, it is important to have a detailed information about the modification of PSi induced by heating in oxidant atmosphere. For this reason, we investigated the isoconversional kinetics of thermal oxidation of mesoporous silicon [3]. By this study, we could obtain detailed insight about the oxidation process and the values of the activation energy of the oxidation steps.

References

1. Ghafarinazari, M. Scarpa, G. Zoccatelli, M. Comes Franchini, E. Locatelli, N. Daldosso Hybrid luminescent porous silicon for efficient drug oading and release. RCS Adv. 2017, 7, 6724-6734.
2. Lion, N. Laidani, P. Bettotti, C. Piotto, Pepponi G., Barozzi, M. Scarpa, Porous silicon platforms providing hydrophilic surface and hydrophobic cavities. Manuscript in preparation.

3. Ghafarinazari, E. Zera, A. Lion, M. Scarpa, G.D. Sorarù, G. Mariotto, N. Daldosso Isoconverional kinetics of thermal oxidation of mesoporous silicon, Thermochimica Acta 2016, 623, 65-71.

5. Asymmetric Mach-Zehnder Interferometer based biosensor for Aflatoxin M1 detection in milk (Tatevik Chalyan)

Since November 2013, the Nanoscience Laboratory is involved in the European Project SYMPHONY. The project aims to produce a platform that enables the rapid detection of toxins and contaminates, with an initial focus on the carcinogen Aflatoxin M1 (AFM1), in milk and milk products. The miniaturized smart system will perform label free detection of contaminants in milk and improve safety and quality of dairy products. The main goal is to produce an automated sampling and analysis system to be used at intake lab in dairies.

High-resolution biosensors, such as SiN asymmetric Mach-Zehnder interferometers (aMZI developed by LioniX) and SiON microring resonators (MRR developed by FBK), were studied for analyte detection. Both types of sensors gave good results in terms of sensitivity, Limit of Detection and reproducibility. The aMZI solution was selected for final implementation because it was demonstrated to be more suitable for integration. In order to ensure the repeatability of AFM1 sensing Fab' functionalization has been chosen.

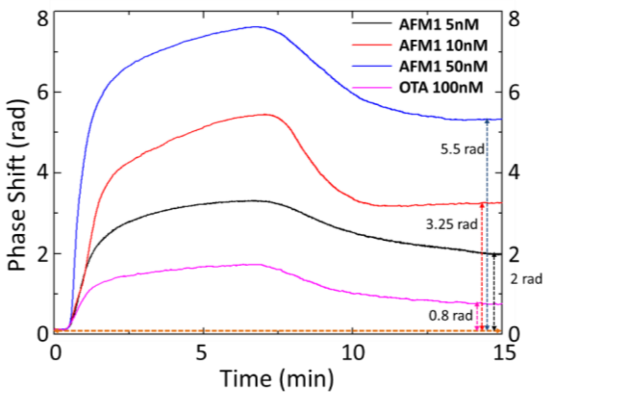

Figure 8. *Sensing measurements of 5 nM, 10 nM and 50 nM pure AFM1 and 100 nM OTA diluted in MES performed using four different aMZI based chips functionalized with Fab' antibodies. The flowing buffer is MES. Sensorgram shows the phase evolution when the solution with AFM1 flows over the sensors.*

To determine the lowest detectable AFM1 concentration, we performed measurements with different concentrations of AFM1. Figure 8 shows the results for 50 nM, 10 nM and 5 nM AFM1 concentrations in MES buffer. All the three exposed aMZI on the same photonic chip demonstrate similar phase shifts. Considering the molecular weight of AFM1 of 328.27 g/mol, 5 nM corresponds to 1.5 ng/mL. This value is higher than the value permitted by European regulations (50 ng/L in milk). In order to decrease the limit of detection of the sensor, a pre-concentration module is needed. To be sure that the achieved signals are due to the AFM1 binding, we did measurements to prove the specificity of our sensors. For this purpose we used OTA at 100 nM concentration. Fig. 8 shows that even though the concentration of OTA is significantly higher than concentrations of AFM1, the non-specific signal is much lower in comparison with specific signal. The functionalization is shown to be specific. In fact, in the case of AFM1 at 5 nM, after MES rinsing, the phase shift is 2 rad, while for OTA it reaches 0.8 rad.

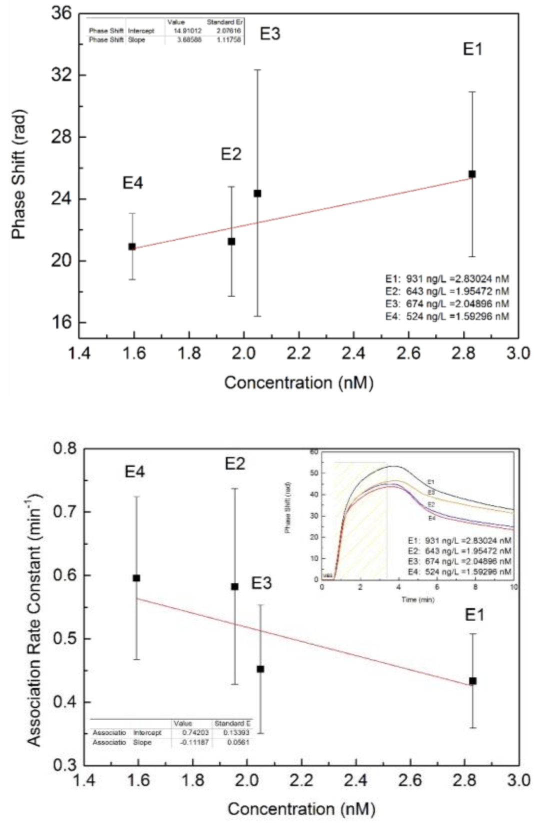

Figure 9. *(a) Dependence of the phase shift on the concentration of AFM1 in eluate. (b) The dependence of the association rate constant (k) on the concentration of AFM1 in a time range of t=0.7'÷ 3.4'. Only results from the first injections are used to calculate k.*

Finally, we measured real contaminated milk samples (eluates) that have been defatted and concentrated in MES buffer before sending to the sensor. The contaminated eluates were previously characterized by ELISA analysis for AFM1 content. Four different chips were tested. Between each injection of eluate, a regeneration process with glycine solution was performed. We found a clear trend as a function of AFM1 content that points to a sensor response for the contaminated eluates. In order to quantify the sensor response, the dependence of the phase shift and association rate constant from the AFM1 concentration are presented in Fig. 9(a) and Fig. 9(b) respectively. The phase shift is taken at t=10', and the association rate constant is calculated in the range of t=0.7'÷ 3.4'.

6. Analytical modelling of whispering gallery mode resonators (Foroogh Khozeymeh)

Whispering Gallery Modes (WGMs) are the electromagnetic resonances inside an axis-symmetric dielectric waveguide such as microsphere, micro-disc, micro-cylinder and micro-bottle. For practical applications of WGM resonators, first we have to compute the WGMs. This we do by solving the electromagnetic wave equations in the specific geometry we are interested in. Here we are using a novel approach, Lam analytical expansions, to get analytical closed form of WGMs resonances in a two layer cylindrical resonator. The Lam expansion, which was used for spherical resonators in the past, is here generalized to cylindrical resonators. Thus, we are able to compute analytical closed form of WGM wavelengths with different radial and angular orders, (with both polarization TE and TM).

$$n_c x_l{}^i = \nu + \frac{\alpha_i}{2^{1/3}}\nu^{1/3} - \frac{mp}{\sqrt{m^2-1}} + \frac{3\alpha_i}{10\times 2^{2/3}}\nu^{-1/3}$$
$$+\frac{m^3 p(\frac{2p^2}{3}-1)\alpha_i}{2^{1/3}(m^2-1)^{3/2}}\nu^{-2/3} + o(\nu^{-1}),$$

where $\nu = l + 1/2$, $m = n_c/n_e$ is the relative refractive index between the cylinder and the contact medium, and x_i is the *i-th* zero of the Airy function and represents the radial order of WGMs. Another analytical method, which has been successfully applied to planar WGM resonators, is the Conformal Transformation Method (CTM). With this method, it is possible to compute the effective index of the resonator WGM. CTM transforms a curved resonator into an equivalent straight waveguide and, in comparison with numerical methods, provides a deep physical insight into the mode properties. The essence of the CTM is to assume a spatial dependent refractive index. As an example, for TE polarization and using the transformations:

$$W = u + iv = f(Y) = f(x,z)$$
$$W = R_2 \ln Y/R_2$$
$$\left|\frac{dY}{dW}\right| = \exp(u/R_2)$$

the wave equation becomes:

$$\left[\nabla_{u,v}{}^2 + \left|\frac{dY}{dW}\right|^2 \frac{\omega^2 n^2(x(u,v),z(u,v))}{c^2}\right] e_Y(x,z) = 0$$

the solution of which is the wavefunction looked for..

7. Automatic resonance alignment of a double–ring based optical switch node (Stefano Tondini)

Project IRIS (http://www.ict-iris.eu) aims at creating a highly integrated, scalable, transparent and high capacity wavelength-division-multiplexing Photonic Switch (PS) to be used as a transponder aggregator to existing Reconfigurable Optical Add Drop Multiplexer (ROADM) nodes. In view of this challenge, we are developing an automated method to calibrate the thousand micro-ring resonators (MRRs) of the PS, compensating for production inaccuracies. Each optical node of the PS is made of two MRRs evanescently coupled to the bus waveguides, as shown in Fig.10 (a). By means of the thermo-optic effect it is possible to tune the optical node to a desired wavelength. In fact, the MRRs are provided with dedicated metallic heaters, which can be operated independently in order to overcome the misalignment of the MRRs resonances due to fabrication errors.

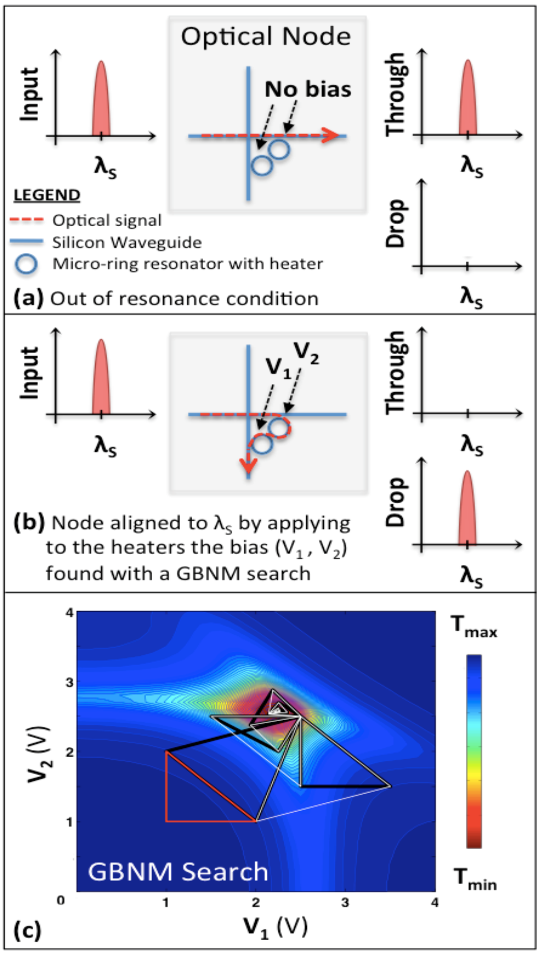

Figure 10 *(a)-(b) Initial and final condition in the alignment procedure of the double-MRR optical node. (c) One iteration of the GBNM algorithm executed to find the bias voltages needed to obtain the minimum optical power in the through port of the node. The red triangle is the starting configuration, while the evolution of the search is represented by alternating black and withe triangles. The contour plot on the back of the plot has been obtained, on the same node, by searching the entire domain of the possible bias configurations.*

Few strategies have been already proposed to automatically align the resonance of a MRRs based optical node in a selected spectral position [1]. Among those, the Nelder-Mead (NM) is the most suitable heuristic method for performing local optimization in a low number of steps [2]. For our purpose, we decided to implement an improved version of the NM, called Globalized Bounded Nelder-Mead (GBNM), which accounts for variable bounds and is particularly robust against stagnation at non-optimal solutions [3,4]. The algorithm combines the NM method (local optimizer) to a random search (global optimizer). The globalization is achieved through probabilistic restarts: a probability function keeps a memory of past local searches and pushes the new search to the regions far from already-found solutions. This stochastic optimization algorithm finds the wanted pass-band over multiple instances, preventing the convergence solution to be trapped into local attraction basins of the search domain (i.e., wrong solutions of the problem at hand).

In our experiment, a tunable laser (set to the wavelength at which the node has to be aligned) is coupled with the input port of the node. With no bias applied to the heaters, the optical signal is expected to be maximum at the through port (Fig.10(a)). When the MRRs heaters are biased, a feedback controller, which implements the GBNM search (Fig. 10(c)), finds the set of voltages (V_1,V_2) that minimizes the optical power at the through port of the node (Fig. 10(b)). This way, the MRRs resonances match, and the selected wavelength is coupled with the drop port.

References

1. Mak, Jason CC, et al.: 'Automatic resonance alignment of high-order microring filters', IEEE Journal of Quantum Electronics, 2015, 51.11, pp. 1-11
2. Nocedal, J., Wright S.: 'Numerical optimization', Springer Science & Business Media, 2006
3. Luersen, M. A., Le Riche, R.: 'Globalized Nelder–Mead method for engineering optimization', Computers & structures 2004, 82.23, pp. 2251-2260
4. Kelley, C. T., 'Detection and Remediation of Stagnation in the Nelder–Mead Algorithm Using a Sufficient Decrease Condition', SIAM Jour. on optimiz., 1991, 10.1, pp. 43-55.

8. Bond orbital description of strain induced second order nonlinearity in silicon (Astghik Chalyan)

Silicon belongs to the class of centro-symmetric materials, and so it has no native $\chi^{(2)}$. Since also $\chi^{(4)}$ vanishes, it comes out that the dominant nonlinearity in silicon is the third order non-linear susceptibility $\chi^{(3)}$. However, we demonstrated that $\chi^{(2)}$ effects can be induced by applying strain gradients.
Different attempts aim to create a model to describe the relation of $\chi^{(2)}$ to the induced strain. One connects $\chi^{(2)}$ to the deformation by the silicon deformation potentials [1]. The deformation potentials theory relies on the de-localisation of the Bloch wavefunction over the entire crystal. When applied to the description of nonlinear optical phenomena in inhomogeneously strained media, its description of the effects is very limiting because it is not a local theory [2]. The goal of our work is to perform an ab-initio calculation of the second-order nonlinear optical response of strained bulk silicon using the bond orbital theory. In particular, we aim to build upon the model described in [3] to analyze the experimental measurements taken in our laboratory on Second Harmonic Generation in strained silicon waveguides. The model is based on the assumption that the bulk silicon centro-symmetry can be broken by moving the silicon atoms in the lattice, which means by modifying their bond energy. It is known that $\chi^{(2)}$ depends primarily on the polarity of the bonds of the crystal, which is the difference of energy between the two electrons in the bond. In a centro-symmetric crystal, a homogeneous strain changes the energy of the bonding electrons, but it is still the same in both sides of the bond, maintaining the inversion symmetry. However, if there is a strain gradient in the direction of the bond, the atomic configuration changes and a bond becomes polar. This fact explains why inhomogeneous strain fields are required to induce bond polarity and thus $\chi^{(2)}$.

Following the work done in [3], the spatial distribution of $\chi^{(2)}$ in the crystal can be expressed as:

$$\chi^{(2)}_{ijk} = \sum_{lmn} \Gamma^{ijk}_{lmn} \eta_{lmn}$$

where η_{lmn} is a generic strain gradient component related to the strain component by: $\eta_{lmn} = \partial\varepsilon_{ij}/\partial x_k$. This means that $\chi^{(2)}$ is defined by the contribution of strain gradients and by the Γ coefficients. The components of the strain gradient can be found by FEM simulations. On the other side, the values of Γ can be uniquely determined by the bond orbital description, which relates Γ to only two parameters α and β. These parameters are related to the crystal potential V as follows:

$$\alpha \sim \frac{1-\gamma}{2d}\left(\frac{\partial V}{\partial r}\right)_d \qquad \beta \sim -\frac{1}{d}\left(\frac{\partial V}{\partial r}\right)_d$$

being γ and d factors related to the geometry of the bond. Taking the potential V from literature, the parameters α and β and, then, $\chi^{(2)}$ can be determined.

References

1. S. V. Govorkov, V. I. Emel'yanov, N. I. Koroteev, G. I. Petrov, I. L. Shumay, V. V. Yakovlev, and R. V. Khokhlov. Inhomogeneous deformation of silicon surface layers probed by second-harmonic generation in reflection. J. Optical Society of America B, 6(6), 1117 (1989).
2. NK Nick K. Hon, Kevin. K. KK Tsia, Daniel R. DR Solli, Bahram Jalali, and Jacob B. Khurgin. Stress-induced χ(2)in silicon—Comparison between theoretical and experimental values. In 6th IEEE International Conference on Group IV Photonics, pages 232–234 (2009).
3. P. Damas, D. Marris-Morini, E. Cassan, and L. Vivien. Bond orbital description of the strain-induced second-order optical susceptibility in silicon. Physical Review B, 93(16), 165208 (2016).

9. Second harmonic generation in strained silicon waveguides (Alessandro Marchesini, Alessandro Trenti, Mattia Mancinelli, Claudio Castellan)

Since silicon exhibits a centrosymmetric crystal structure, the nonlinear second order coefficient $\chi^{(2)}$ is null. However, $\chi^{(2)}$ effects are desirable in silicon in order to develop fast and low cost electro-optic modulators. To achieve a non-vanishing $\chi^{(2)}$, a breaking of the centrosymmetry is required. In [1] Second Harmonic Generation (SHG) measurements were reported in large cross section Si waveguides, where the breaking of the Si symmetry was obtained by the deposition of a stressing silicon nitride over-layer on the top of the waveguide. However, the SHG data were affected by different contributions caused by the interfaces, the free carrier induced internal electric fields, the inhomogeneous strain and the uncontrolled modal structure of the waveguides.
In this work we present SHG observation in Silicon On Insulator (SOI) strained Si waveguides, whose geometry was chosen to maximize the generation efficiency and to satisfy the phase-matching condition: $n_{eff}(\lambda_p) = n_{eff}(\lambda_p/2)$ (n_{eff} is the effective refractive index and λ_p is the pump wavelength). Since the refractive index is dispersive, the last condition is never satisfied by the same optical mode. However, it can be satisfied by different optical modes, in a modal phase

matching scheme. In our experiment, we analyzed SOI waveguides with different widths around 2 µm, an height of 250 nm and a 140-nm-thick silicon nitride overlayer which induces a measured tensile stress of +1.25 GPa. We used a model for the simulation of the pulse-propagation in waveguides to estimate the experimental conditions able to maximize SHG, limiting dispersive effects (such as walk-off) and third order nonlinear effects (such as self-phase modulation). To perform the measurements, we used a ~70 fs tunable laser with 1 kHz of repetition rate. The temporal width of the pulses was reduced to ~13 ps using a pulse-shaper. In this way, the walk-off effect was reduced and the peak power was reduced to limit the self-phase modulation. The operating pump wavelengths were in the range (2.4 : 2.6) µm to eliminate the generation of free carriers by two photon absorption.

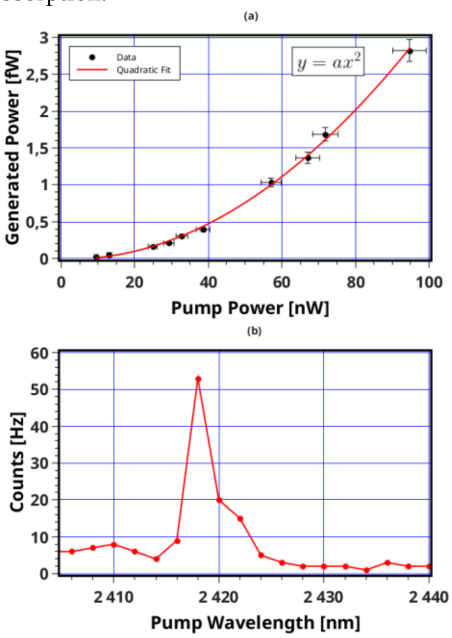

Figure 11. *(a) Generated SHG power, as a function of the input pump power. The pump wavelength for the generation is 2.418 µm. The waveguide width is 2.25 µm and its length is about 1.8 mm. (b) Generated SHG signal as a function of the pump wavelength.*

The results are shown in Fig. 11. The generated power exhibits a quadratic dependence on the pump power, as it is expected from the theory. The optical modes involved in this process are the fundamental TE mode for the pump and the fifth order TM mode for SHG. We estimated a strain induced second order nonlinearity of $\chi^{(2)} = (0.304 \pm 0.025)$ pm/V, which is in agreement with the results coming from high frequency measurements of Pockels effect in strained silicon [2]. However, this value is an underestimation, since we figured out that random fluctuations of the waveguide width, due to the lithography resolution limit, lead to a drop in SHG efficiency. According to the simulation, the SHG bandwidth (Fig. 11(b)) is about 5 nm.

The observation of SHG is very interesting, since it provides a milestone for the observation of Spontaneous Parametric Down Conversion (SPDC) in strained silicon waveguides. In the SPDC process, two entangled photons are generated at a doubled wavelength with respect to the single pump photon. In recent years, great interest has been devoted to move quantum optic applications to the MIR, due to the easy of photon manipulation in that spectral region. Therefore, the possibility of generating MIR entangled photons in a strained silicon waveguide pumping at telecom wavelengths provides an interesting future perspective for this work.

References

1. M. Cazzanelli et al., "Second-harmonic generation in silicon waveguides strained by silicon nitride", Nat. Mater. 11, 148-154 (2012).
2. M. Borghi, M. Mancinelli, F. Merget, J. Witzens, M. Bernard, M. Ghulinyan, G. Pucker, L. Pavesi, "High frequency electro-optic measurement of strained silicon racetrack resonators", Opt. Let. 40, 5287 (2015).

10. Counter propagating Four Wave Mixing in silicon waveguides (Stefano Signorini, Mattia Cominelli, Mattia Mancinelli)

Four Wave Mixing (FWM) is one of the most used nonlinear optical processes for on-chip entangled photon generation, wavelength conversion, Optical Parametric Amplification and Optical Parametric Oscillation (OPO) [1]. FWM in optical waveguides is usually studied in a geometry where all the waves propagate in the same direction (co-propagating geometry). However, FWM can occur also when the pump, signal and idler photons counter propagate inside the medium [2]. Currently, we are studying the occurrence of counter propagating degenerate sFWM in a multimode silicon channel waveguide, with both experimental measurements and simulations. The counter propagation in our waveguide is due to the reflections occurring at the silicon/air interface characterizing the input and output facets of the waveguide.

While in the co-propagating FWM two co-propagating pump photons are nonlinearly converted into two co-propagating signal and idler photons, in the counter propagating FWM, Fig. 12(a), two counter propagating pump photons ($h\nu_p$) are converted into two counter propagating signal ($h\nu_s$) and idler ($h\nu_i$) photons.

The counter propagation geometry affects the phase matching condition that becomes [2]

$$k_p - k_p = k_s - k_i \Longrightarrow k_s = k_i \qquad (1)$$

where k_p, k_s and k_i are the wavevectors of, respectively, the pump, the signal and the idler photons. The efficiency of FWM is maximized when the phase matching condition is satisfied, and the great advantage of the counter propagating FWM is that the phase matching condition is satisfied for any pump wavelength in a wide wavelength range [2]. This can be seen in (1), since the phase matching condition does not involve the pump photons.

We numerically simulated the counter propagating sFWM with higher order waveguide modes selection. The dispersion of the multi-modes involved in the process selects the wavelength of the generated signal [3]. We used a Silicon-On-Insulator (SOI) channel waveguide, with 3.6 µm width, 250 nm height and 1.5 cm length. To excite the higher order modes in the waveguide we injected the pump and the stimulating idler in the waveguide with an optical fiber that was tilted by an angle with respect to the input facet of the waveguide. The pump was a pulsed laser at 1550 nm. The stimulating idler was a continuous wave laser.

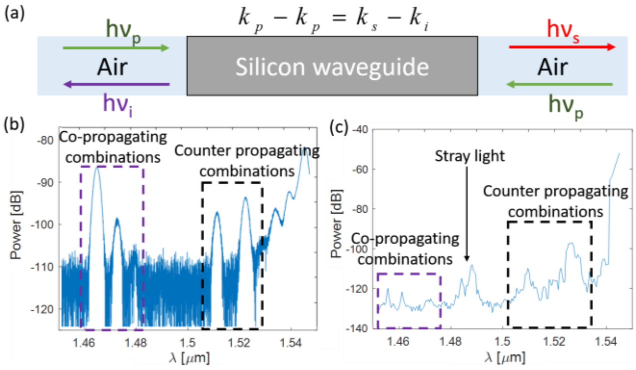

Figure 12. *(a) Scheme for the propagation of the photons involved in the counter propagating FWM. Simulation (b) and experimental measurement (c) of the generated peaks through sFWM in the silicon waveguide under study.*

Fig. 12(b) and Fig. 12(c) report, respectively, the simulation and the experimental measurement of the generated signal peaks via FWM. Each peak refers to a different modal combination for the waves involved in the process. Without considering the counter propagating combinations, the measured peaks near to 1510 nm and 1530 nm in Fig. 12(c) cannot be explained. Slight differences between simulation and experiment are due to fabrication imperfections of the waveguide.
The experimental measurement in Fig. 17(c) suggests that the counter propagating combinations exhibit higher efficiencies than the co-propagating ones. The experimental demonstration of counter propagating FWM could open new possibilities for applications involving stimulated and spontaneous FWM [4].

References

1. J. Leuthold, C. Koos, and W. Freude, (2010). Nonlinear silicon photonics, Nature Photonics, 4(8):535-544, 2010.
2. Yan, Y., Zhang, L., & Willner, A. (2011). Nondegenerate mirrorless oscillation in silicon waveguide. Optics letters, 36(20), 4113-4115
3. Fernandes, G. M., Almeida, Á. J., Niehus, M., et al., (2013). Theoretical analysis of multimodal four-wave mixing in optical microwires. Journal of Lightwave Technology, 31(2), 195-202.
4. Monroy-Ruz, J., Garay-Palmett, K., et al. (2016). Counter-propagating spontaneous four wave mixing: photon-pair factorability and ultra-narrowband single photons. New Journal of Physics, 18(10), 103026.

11. Spontaneous FWM and coincidence measurement (Massimo Borghi, Mattia Cominelli)

In the last decade, quantum technologies, i.e, devices which exploit quantum mechanical effects to beat the classical limit, are receiving growing attentions [1]. One of the most promising platforms are quantum integrated circuits. Here, the fundamental building block is the source of nonclassical states of light to be processed on chip. At the early stages, this task was accomplished by external sources based on Spontaneous Parametric Down Conversion occurring in bulk nonlinear crystals. A high power laser to ensure sufficient brightness pumped these. Over the years, the research rapidly moved towards integrated sources, which are inherently scalable, offer improved stability, and take the advantage of the ultra-high intensities in photonic nanowires to enhance optical nonlinearities. We are investigating Spontaneous Four Wave Mixing (SFWM) in Silicon On Insulator microring resonators as a source of correlated photon pairs. In this experiment, we resonantly inject pump photons at 1550 nm with sub-milliwatt power at the input of a 7 μm radius resonator. The pump intensity is enhanced due to the resonant structure by approximately a factor of ten. The $\chi^{(3)}$ of Silicon made pairs of pump photons at frequency ω_p to annihilate, generating signal and idler photons at frequencies ω_s and ω_i. These satisfy the energy conservation relation $2\omega_p = \omega_s + \omega_i$. The correlation in energy, and the large coherence time of the pump, spectrally filtered by the high-Q resonator, lead to the generation of a two-photon state, which is highly not separable and is said to be time-energy entangled.

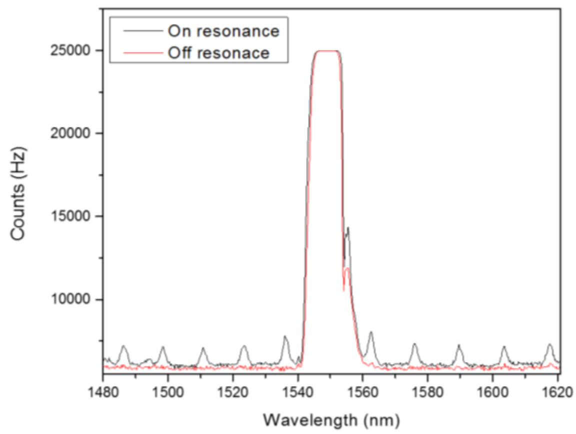

Figure 13. *Spontaneous FWM in the microring resonator. The black line is recorded with the pump laser tuned on resonance, while the red line is recorded with the pump laser blue detuned by* $\sim 0.2\ nm$ *with respect to the resonance wavelength.*

Fig.13 shows an example of the spectrum of the light collected at the output of the resonator, when a 2 mW pump power is coupled into the chip. This spectrum has been recorded by a homemade, double-pass, free space monochromator coupled to an InGaAs photon counter. The high central peak is due the residual of the pump laser, which was previously filtered by more than $100\ dB$ from the other wavelengths. The side peaks, located exactly at the resonances of the microring, are associated to signal/idler pairs generated by SFWM. Due to the low group velocity dispersion of the waveguide, the efficiency of the spontaneous process maintains quite flat over the investigated spectral interval, leading to a comb of entangled photon pairs which extends by more than $100\ nm$. It is worth to note that the peaks disappear when the pump wavelength is tuned off-resonance, demonstrating that they arise from a resonant process. We made a correlation measurement of the arrival times of the signal/idler photons at two different photodetectors. Indeed, a clear signature of time-entanglement is the fact that the two photons are emitted at the same time. The result, shown in Fig.14, reveals a clear coincidence peak at zero delay, which raises over a constant background. From this measurement, we extracted an on-chip generation rate of 7.8 MHz, mainly limited by Two Photon Absorption. This value is comparable to the state of the art [2]. We are currently working to improve the signal to noise ratio in order to enable further on chip manipulation of these photons.

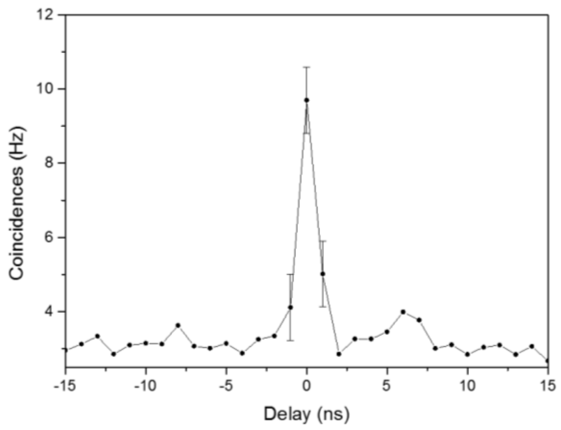

Figure 18. *Coincidences of the arrival times of the signal and idler photons as a function of the time delay between them. The integration time is 100 s.*

References

1. V. Giovannetti, S. Lloyd, and L. Maccone, "Quantum-enhanced measurements: beating the standard quantum limit", Science, vol. 306, pp. 1330-1336, (2004)
2. S. Azzini, D. Grassani, M.J. Strain, M. Sorel, L.G. Helt, J.E. Sipe, and D. Bajoni, ,"Ultra-low power generation of twin photons in a compact silicon ring resonator". Opt. Express, vol. 20, pp. 23100-23107, (2012).

12. Design and simulation of quantum photonic circuits (Massimo Borghi)

Photons are attractive for encoding and transferring informations for applications like quantum computing, quantum cryptography and quantum communication. Indeed, they suffer from reduced decoherence with respect to atoms, and they allow for many degrees of freedom for entanglement, such as polarization, frequency and spatial mode distribution [1]. In the last few years, Silicon On Insulator quantum integrated optical circuits have been demonstrated to be effective candidates for realizing quantum technologies, due to their compactness, reduced loss, ease of use and availability of bright, stable, non-classical light sources. A complete quantum circuit includes a photon source, a reconfigurable network, capable of realizing arbitrary linear and nonlinear transformation on the input state, and a detection stage. Integrated quantum sources have been demonstrated both in spiral waveguides and in microcavities, based on Spontaneous Four Wave Mixing. Complex linear networks, including hundreds of splitters and heaters, have been demonstrated to be capable of realizing any unitary transformation between the input and the output state of the system [2]. Integrated single photon detectors, mainly based on gold Superconducting Nanowires, still present some yield challenges, but are on the way to become standard technologies for on-chip photodetection [3]. In our work, we are developing a fully reconfigurable quantum circuit, where frequency entangled photon pairs are generated, spectrally filtered from the pump, and manipulated on chip. A sketch of a section of the whole circuit is shown in Fig. 19.

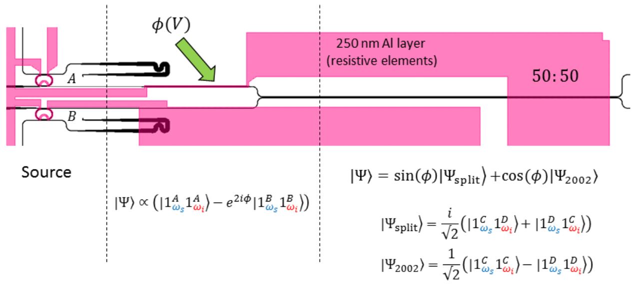

Figure 19. *A sketch of the quantum state preparation stage. From left to right: racetrack resonators photon sources and reconfigurable heater with 50/50 splitter. Under each section, the evolution of the quantum state is indicated. A(B) labels the upper(lower) waveguide,* ω_s *and* ω_i *the signal and the idler photon, and* ϕ *the relative phase between the channels A and B imparted by the heater.*

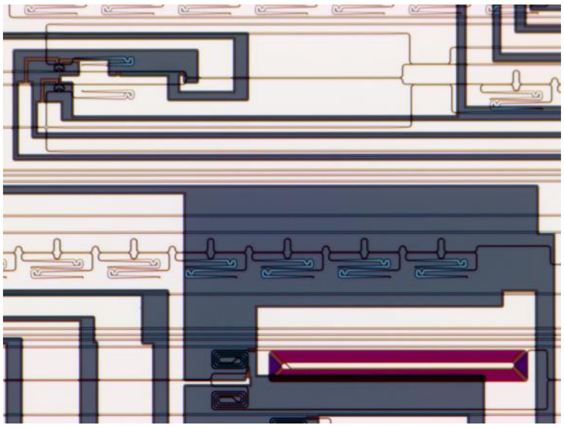

Figure 20. *Optical microscope image showing some of the fabricated devices. The white parts are Aluminum traces which connect the micro-heaters to external bonding pads. These are used to externally reconfigure the circuit. The dark red lines over the grey background are the Silicon waveguides. This picture is a courtesy of Mher Ghulynian (Advanced Photonics & Photovoltaics, Fondazione Bruno Kessler, Trento, Italy).*

Light from a single input waveguide is split, and excites two racetrack resonators, which have been engineered to generate 1 MHz signal/idler photon pairs with 1 mW of input pump power. With such low level of input power, only one of the two sources will generate a pair, but since they are made indistinguishable, we will have a superposition of these possibilities at the output. Photons will be bunched into one or into another channel, with equal probability. The associated quantum state is called N00N (in this case, N=2). With the use of a splitter and a heater, we can then deterministically keep the photons bunched together, or change the state into an antibunching one, in which we have one photon into one spatial mode, and another into a different spatial mode. The pump isolation is also realized on chip. We implemented cascaded Mach-Zehnder interferometers to achieve a theoretical suppression efficiency of 120 dB.

We then designed additional stages in which two photon interference can be observed. These includes Hong Ou Mandel interferometry with non-degenerate photon pairs and Franson interferometry. In some of these experiments, the photons have to be spectrally separated before being detected, or one has to induce a tunable delay to one photon with respect to the other. This is respectively achieved by integrated Arrayed Waveguide Gratings and slow light structures such as cascaded sequences of resonators. The chip is currently under fabrication (see Fig. 20), and we are planning to test it in the next few months.

References

1. Politi, M.J. Cryan, J.G. Rarity, S. Yu, S.,and J.L. O'brien, “Silica-on-silicon waveguide quantum circuits”, Science, vol. 320, pp. 646-649, (2008).
2. J. Carolan et al., "Universal linear optics", Science, vol. 349, pp. 711-716, (2015).
3. N.C. Harris et al., "Large-scale quantum photonic circuits in silicon", Nanophotonics, Vol.5, pp. 456-468, (2016).

13. A coincidence measurement on twin photons in the Mid-Infrared region (Sara Piccione, Alessandro Trenti, Mattia Mancinelli)

In recent years, an intense area of research of the Nanoscience Laboratory has been quantum optics, where coincidence detection of photon pairs plays a central role. In particular, during the last year, a room temperature coincidence measurement with non-degenerate twin photons at about 3.1 µm, produced by the nonlinear process of Spontaneous Parametric Down Conversion (SPDC), was achieved. To our knowledge, the obtained result was the first successful attempt towards the extension of quantum optics experiments in the Mid-Infrared (MIR) spectral region. The success of the experiment was possible thanks to the established collaboration between the NL group and the Danmark Tekniske Universitet (DTU), which developed a novel up-conversion system for the MIR single photon detection [1]. Indeed, what really makes MIR single-photon experiments elusive is the lack of high sensitivity detectors. MIR detectors had faced many limitations, mainly due to their inherent sensitivity to the black body radiation and dark current induced by the finite temperature of the detector itself. In principle, the noise could be reduced by cooling the detector down to the liquid nitrogen temperature, but the signal-to-noise ratio remains poor compared to NIR and visible light detectors.

We approached the problem differently by using the concept of spectral translation. The idea is to up-convert the infrared radiation in the visible domain by means of optical nonlinear effects. The up-conversion module is shown in Fig. 19. It comprises of two distinct parts. First, the up-conversion crystal which is a 20mm long PPLN fabricated for Sum Frequency Generation (SFG) between a 1064 nm pump laser beam and an incident radiation in the 3 µm wavelength range. The crystal has five poling periods ranging from 21 µm to 23 µm in steps of 0.5 µm, to obtain the phase matching condition.

Second, the nonlinear crystal is placed inside a high finesse 1064 nm laser cavity in order to enhance the up-conversion probability. Up to about 100 W of continuous-wave circulating laser power can be achieved, providing an increase by about 100 times in the Conversion Efficiency.

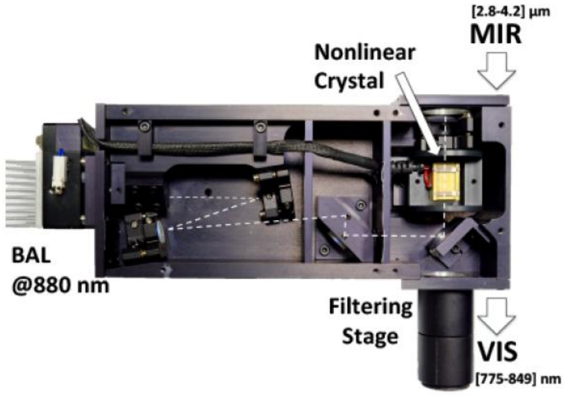

Figure 21. *Photograph of the up-converter module.*

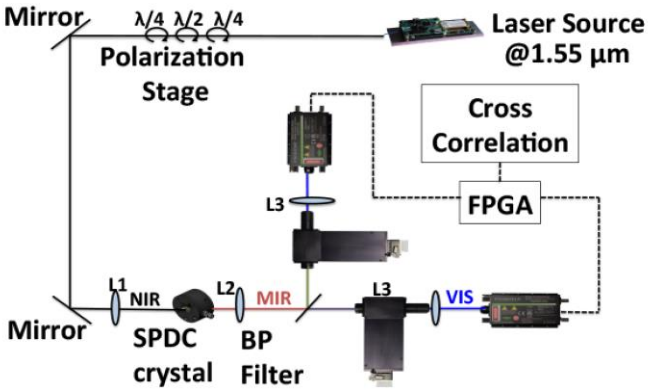

Figure 12. *Sketch of the experimental set-up for coincidence measurement in the MIR*

The experimental set-up for the coincidence measurement is shown in Fig. 22. It consists of a fiber-coupled, continuous-wave laser with tuning range from 1.52 µm to 1.56 µm and a maximum output power of 70 mW. The laser source is amplified using an Erbium-Doped Fiber Amplifier, with a maximum output power of 800mW. The polarization is controlled through a stage composed by two quarter-wave plates and one half-wave plate. Then, the pump beam is focused into a periodically poled PPLN crystal, pumping the SPDC process. The two generated photons are then split and directed to the two up-conversion modules, thanks to an IR optical bandpass filter centered at 3 µm, with a bandwidth of 250 nm. The idler wavelength at 3.343 µm is reflected and the signal photon at 2.89 µm is transmitted through the bandpass filter. Residual pump photons at 1.55 µm are eliminated by a Germanium window, placed at the entrance of each of the up-conversion modules. The up-converted photons are detected using silicon based single-photon counters. They achieve a peak photon detection efficiency of about 65% at 792 nm over a 180 µm diameter with unmatched uniformity over the full active area, each coupled to an up-converter module.

The total loss from the output facet of the SPDC PPLN to the single-photon detector has been estimated to be 25 dB. 10 dB comes from the conversion efficiency of both the up-

converter modules. The remaining losses are due to a non-perfect overlap with the active area of the silicon detector. The output TTL voltage of the Si SPADs is fed into a Field Programmable Gate Array (FPGA) digital correlator that provides the coincidence rate. The FPGA is programmed to make a real-time cross correlation between the TTL signals of the two Si SPADs. The coincidence window is 1.33ns.
A clear peak of coincidences in time between the signal and idler has been observed, as reported in Fig. 23, which demonstrates the time-correlated nature of the MIR generated photon pairs and the capability of our systems to perform this kind of experiment. Ideally, the coincidence peak would appear at a zero delay, but due to small differences in the electronic circuitries, it appears at a delay of 8 ns.

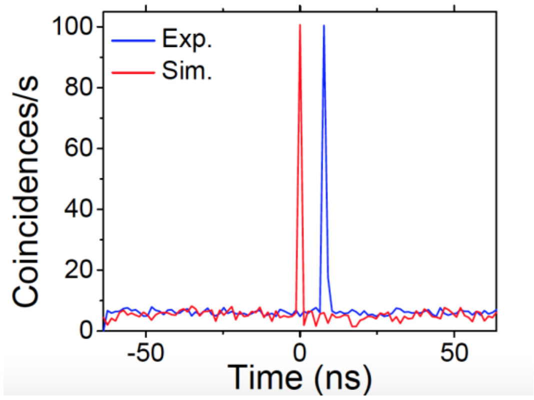

Figure 23. *Coincidence rates, measured (blue line) and simulated (red line) after 10s of integration. The coincidence peak rate is 150±1 cps (counts per second)*

The expected coincidence rate as a function of the count rate and background count rate of each module has been simulated taking also in account the overall losses of the system. The simulated result (solid red curve in Fig. 23) is comparable with the experimental result (solid blue curve in Fig.23).
In conclusion, we have presented a room temperature coincidence measurement of mid-infrared entangled photons. To our knowledge, this is the first demonstration of this kind of measurements in the MIR spectral range. Our detection system outperforms other currently available MIR detection systems, in particular those based on superconducting technology. This is a key result, since coincidence measurements is the standard technique nowadays for photon pair detection, which is at the core of quantum optics experiments and it is especially useful in quantum communication protocols based on entangled photons.

References

1. Jeppe Seidelin Dam, Peter Tidemand-Lichtenberg and Christian Pedersen, "Room temperature mid-infrared single-photon spectral imaging", Nature Photonics, 6, (2012).

14. Modeling of Bogoliubov-like dispersion in nonlinear waveguides (Stefano Biasi, Fernando Ramiro Manzano, Fabio Turri)

The quantum fluid of light has been an extensively studied phenomenon in cavity systems. A lot of experiments have been performed in planar microcavity geometries where the presence of strong light-matter coupling allows the observation of its main features (Bose-Einstein Condensation (BEC), superfluid flow, quantized vortices). An alternative optical platform consists in cavity-less nonlinear systems. Our attention is focused on integrated single-mode Silicon or Silicon Nitride waveguides. In these structures, within the paraxial and slowly varying approximation, the complex amplitude of the optical field is a slowly varying function of space and time, which satisfies a nonlinear Schrödinger equation (NLSE). Exchanging the roles played by the time parameter (t) and the propagation coordinate (z), the NLSE is mathematically identical (neglecting the losses) to the Gross-Pitaevskii equation (GPE) of a dilute atomic BEC. In particular, the complex field A(t,z) corresponds to the one-dimensional wavefunction of the condensate ψ, the inverse of the group velocity dispersion β_2 (GVD) to the particle mass (m) and the nonlinear term (γ) to the particle-particle interaction constant (g).

$$i\,\frac{\partial A}{\partial z} = \frac{\beta_2}{2}\,\frac{\partial^2 A}{\partial t^2} - \gamma\,|A|^2\,A \qquad \text{(NLSE)}$$

$$i\,\hbar\,\frac{\partial \psi}{\partial t} = -\frac{\hbar^2}{2\,m}\,\frac{\partial^2}{\partial z^2}\psi + g\,|\psi|^2\psi \qquad \text{(GPE)}$$

Photons	***Cold atom bosons***
Radiation-axis (z)	Time (t)
longitudinal field (*A*)	Condensate's order parameter (ψ)
γ (nonlinear parameter)	Atom-atom interaction (g)
1/β2 (inverse of the GVD)	Mass (m)

Exploiting such analogy, the well-known nonlinear optical phenomenon of Degenerate Four Wave Mixing (DFWM) can be reformulated in the language of the Bogoliubov theory of Bose matter superfluids. Therefore, the wavevector of a signal beam propagating in the nonlinear Kerr medium plays the role of the Bogoliubov dispersion relation of small excitations traveling on top of a weakly interacting BEC. This dispersion is manifested in the Pump power and detuning dependence of the phase of the signal beam.

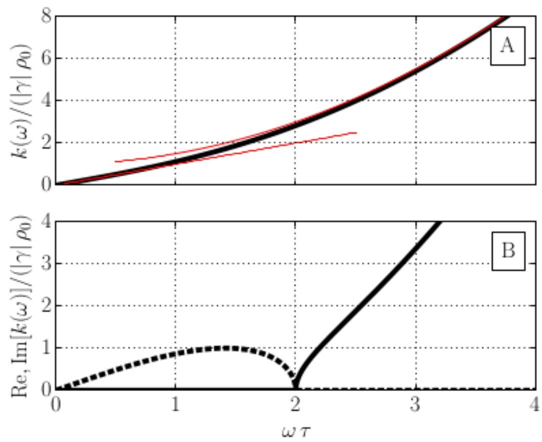

Figure 24. *Theoretical wavevector of the signal as a function of the input frequency. (**A**) Stable regime: the lower (upper) red curve indicates the low-ω (large-ω) linear (parabolic) behavior of the wavevector. (**B**) Unstable regime: the dashed (plain) curve shows the imaginary (real) part of the wavevector.*

The waveguide structure allows designing specific geometries showing different values of the GVD and then different photon effective masses. Moreover, the possibility to achieve different signs of the GVD allows studying both the *stable* and *unstable* regime of the luminous fluid. Actually, when the GVD is normal (i.e. positive photon effective mass) the system is in a stable regime. Here, for large detuning between the signal and the pump frequency, the phase of the signal has a particle character and follows a parabolic shape. On the other hand, small detuning gives rise to a sound-like dispersion (see the linear behavior of Fig. 24). When the GVD is anomalous (i.e. negative photon effective mass) the system can reach an unstable regime. This instability goes under the name of filamentation of the laser beam.
As a side effect, the integration in an optical chip allows achieving a small effective mode area and increasing the accumulated phase by lengthening the waveguide. In our study, the presence of the material losses, such as one and two photon absorption, have been taken into account in both analytical and numerical solutions. Most importantly, we have built a free space Mach-Zhender interferometer to aim at measuring this Bogoliubov-type dispersion relation. This interferometer is fully-automatized and allows performing stable and accurate measurements. Moreover, slightly detuned Pump and Probe signals can be distinguished without any optical filter thanks to a lock-in amplifier.

15. Phase measurements in multimode microring resonators (Fabio Turri, Stefano Biasi, Fernando Ramiro-Manzano)

The interferometric setup [1] implemented within the frame of SiQuro project to verify the analogy between Bose Einstein Condensates and the propagation of a lightbeam in a nonlinear waveguide allows investigating other microresonator properties too. Indeed, the setup is concieved to simultaneously acquire the optical transmittance and the optical phase response of a device provided with input and output ports. The additional information brought by phase measurements allows a deeper comprehension of the investigated system. Thanks to this, different kinds of characterization can be performed on microresonator systems: i) the transfer function at different wavelengths can be obtained; ii) a phasor plot representing the real and imaginary part of the electric field transmitted by the device can be drawn, resembling those observed in electrical engeneering and returning a diffeent view of the resonances present in the device (Fig. 25).
The coupling regime can be accurately investigated on each single resonance, without the need of information on the quality factor or other parameters extracted trough resonance fitting. This is due to the tight relation between phase spectra and resonator losses [2]. In particular, a 2π shift of the optical phase is observed when coupling losses exceeds microresonator internal losses in what is called the overcoupling regime; the opposite coupling regime (undercoupling) presents a phase variation below π and can be easily distinguished from the overcoupled case; similarly, the same regime difference can be recognised through the phasor plot where the presence of a negative imaginary component of the electric field is associated to an over coupling regime of the measured resonance.

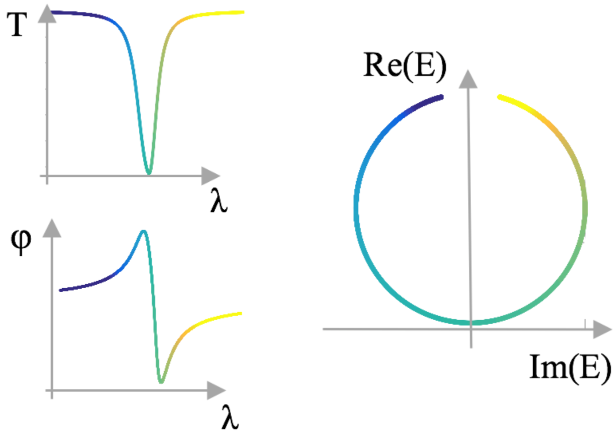

Figure 25. *Transmittance and phase information can be shown through separated plot (left) or condensed in a phasor plot (right); the imaginary and real components of the transmitted electric field are obtained from: Re(E) = T cos(φ) and Im(E) = T sin(φ). Typical specra and phasor of and undercoupled resonance are represented, identified by phase shift below π or by always positive real component of the transmitted electric field.*

On this basis, microresonators showing resonances with Fano lineshape [3], which are occurring in multimode reonators, were studied and the obtained curves were fitted with the model developed in [4] showing good agreement between the experimental data and the theoretical model (see Fig. 26). Thanks to the double information provided by phase and transmittance, accurate identification of the Lamb shift and of the coupling regime of the two coupled families were obtained.

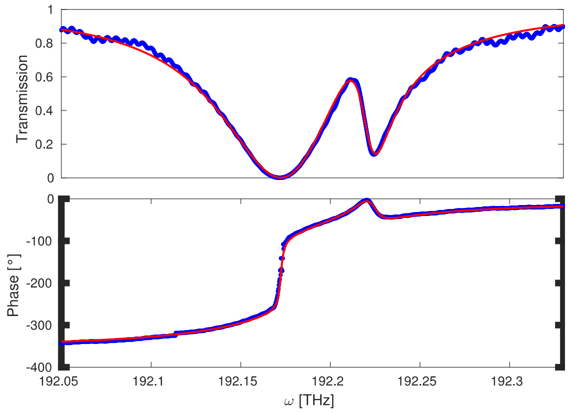

Figure 26. *Transmission and phase spectra of a multimode microresonator showing two coupled resonances. The two spectra are perturbed by rective coupling of the two families. The experiments are fitted with the model described in [3] (red lines). A large phase shift (around 2π) for the broad family and a small one (below π) for the narrow family provide univocal identification of the coupling regime.*

Similarly, the same setup was used to measure the spectra of a multimode resonator showing propagating and counterpropagating modes signature in the near IR range (1300nm), resulting in splitted resonances with Q-factors as high as 10^5. Fitting of the measured data with the most common backscattering models returned good agreement thus confirming the correct operation of the setup.

References

1. F. Turri, *et al.* , submitted to RSI;
2. J. E. Heebner, *et al.*, IEEE journal of quantum electronics, 40(6):726–730, 2004;
3. B.-B. Li, *et al.*, APL **98**, 021116, 2011;
4. M. Ghulinyan, *et al.*, PRA, 90(5):053811, 2014.

16. High-performance SOI AWG for optical network applications (Claudio Castellan, Stefano Tondini, Mattia Mancinelli)

In Wavelength Division Multiplexing (WDM) technology, multiple channels are encoded in a same optical fiber [1]. In this framework, a crucial role is played by the device used at the node of the optical network, where it is required to selectively add and drop optical signals. The realization of these devices on the Silicon-On-Insulator (SOI) platform can take advantage from the mature CMOS technology, which offers the possibility of realizing compact devices available for mass production [2]. With respect to other integrated multiplexing designs, Arrayed Waveguide Gratings (AWGs) do not require ultra-high fabrication processes, offering a good control on the spectral output [3]. In these devices, it is important to keep down the X-talk level, which is the amount of signal that is coupled in the wrong output channel.
In a recent work [4], we evaluated the reduction of the background noise in a whiskered-shaped star coupler (SC). The reflectivity of the SC internal surfaces was modified to reduce the back-scattered light placing a series of inversely tapered waveguides (called whiskers) perpendicularly to the focal lines of the SC. In this way, we showed a reduction in the SC reflectance of more than one order of magnitude. Here we show the effect of whiskers on an entire AWG design.

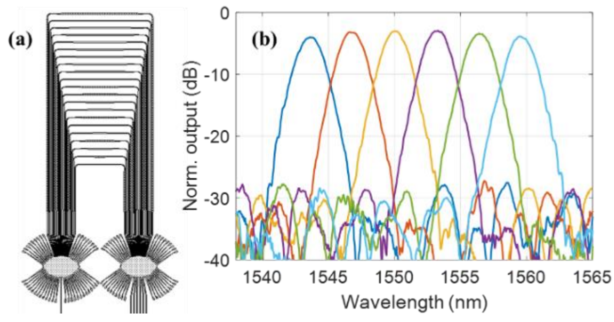

Figure 27. *(a) Sketch of the fabricated AWG. (b) Experimental output spectrum of the 6 channels of the AWG.*

The device analyzed in this work is sketched in Fig. 27(a). It consists in a 1x6 AWG with 400 GHz spacing realized using two whiskered SCs. It is realized with a single etch lithography on a SOI wafer with a 220 nm thick Si layer. The normalized experimental transmission spectrum of the output channels is shown in Fig. 27(b). The measurement is performed using an amplified spontaneous emission source and an optical spectrum analyzer. The AWG performances show a record X-talk level of -25 dB and insertion losses of about -3 dB.

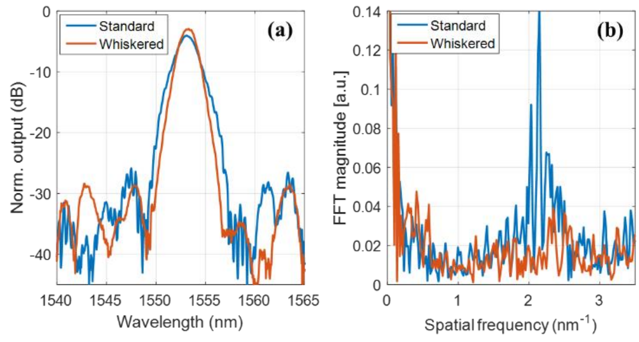

Figure 28. *(a) Comparison between the experimental output spectrum of an AWG with standard SCs and whiskered SCs. (b) FFT of the measured spectra.*

In Fig. 28(a) we compare one of the AWG output channels shown in Fig. 27(b) with the same output channel of a standard AWG, which consists in a device with the same geometric parameters but with SCs without whiskers. We notice that the spectrum of the AWG with standard SCs shows oscillations with a larger amplitude with respect to the ones present in the whiskered device. The same fact is observed by the comparison of the Fast Fourier Transform of the spectra, which is reported in Fig. 28(b) and where peaks at the same spatial frequency but different magnitude are shown. These oscillations have the same origin of those reported in Ref. [4], and are due to Fabry-Perot (FP) interference caused by the SC facets. In the whiskered AWG, the reflectance of the facets is reduced by the presence of the whiskers, thus reducing the amplitude of the FP oscillations. This is confirmed by the agreement between the results coming from the experiment and the theoretical value of the FP spatial frequency for this geometry, which can be calculated using the expression reported in Ref. [4].

References

1. Lee, B.G., Kim, W., ‘Integrated Broadband Networks: TCP/IP, ATM, SDH/SONET, and WDM/Optics’, Artech House, 2002.
2. Dong, Po, et al., ‘Silicon photonic devices and integrated circuits’, Nanophotonics 3(4-5): 215-228, 2014.
3. Pathak, S., et al., ‘Design trade-offs for silicon-on-insulator-based AWGs for (de) multiplexer applications’, Optics letters 38(16): 2961-2964, 2013.
4. Castellan, et al., ‘Reflectance reduction in a whiskered SOI star coupler’, IEEE Photonics Technology Letters 28(17): 1870-1873, 2016.

For more info

Nanoscience Laboratory
Department of Physics
University of Trento
via Sommarive 14
38123 Povo- Trento (Italy)
http://nanolab.physics.unitn.it/

secretary dr. Tanya Yaksevich
email tatsiana.yatckevich@unitn.it
phone +390 461 283172